PAPER • **OPEN ACCESS**

Self-powered solution of synchronous current inversion and energy extraction (SCIEE) for electromagnetic energy harvesting enhancement

To cite this article: Jiacong Qiu and Junrui Liang 2025 *Smart Mater. Struct.* **34** 085016

OPEN ACCESS
IOP Publishing
Smart Materials and Structures
Smart Mater. Struct. **34** (2025) 085016 (11pp)
https://doi.org/10.1088/1361-665X/adf7eb

Self-powered solution of synchronous current inversion and energy extraction (SCIEE) for electromagnetic energy harvesting enhancement

Jiacong Qiu and Junrui Liang*

School of Information Science and Technology, ShanghaiTech University, Shanghai 201210, People's Republic of China

E-mail: liangjr@shanghaitech.edu.cn

Received 12 May 2025, revised 1 July 2025
Accepted for publication 4 August 2025
Published 14 August 2025

Abstract

Self-powered and self-start issues are essential for the standalone applications of switched-mode interface circuits for micro-generators. This paper introduces a self-powered and self-starting solution for small-scale electromagnetic energy harvesters (EMEHs). The self-start solution uses a passive voltage multiplier and an energy buffer-release (EBR) circuit to kickstart the circuit during cold start-up. Introducing an EBR mechanism in the start-up process reduces the required voltage amplitude for cold-start. The EBR circuit features low power dissipation and adjustable thresholds. The operation principle of the proposed EBR circuit is elaborated. The voltage thresholds are theoretically derived and experimentally validated. In experiments, the proposed start-up circuit is applied to the synchronized current inversion and energy extraction circuit, which enhances the harvested power of a low-voltage EMEH. Experiments show that it can start at a relatively low input voltage amplitude, as low as 1.35 V. The total power consumption of the start-up and control circuits accounts for 8.8% of the harvested power at 14 V load voltage. The EBR circuit only dissipates around 46 μW.

Keywords: energy harvesting, self-powered solution, cold start, synchronized switch

1. Introduction

Over the last decades, the Internet of Things (IoTs) technology has grown rapidly. As the number of IoT devices grows, replacing or recharging batteries has become a significant obstacle to deploying and maintaining numerous IoT devices in various scenarios. On the other hand, ambient energy harvesting can power IoT devices to enable self-powered, long-term sensing applications, such as structural health monitoring or marine environment monitoring [1, 2]. One of the electromechanical energy harvesters commonly used in kinetic energy harvesting is the electromagnetic energy harvester (EMEH) [3]. They are also referred to as electromagnetic (EM) generators [4]. Most EMEHs aim at harvesting energy from translational movement [5] and rotational movement [2, 6, 7]. Some studies also use frequency-up conversion mechanisms to convert translational movement into high-speed rotational movements [8, 9] for better generation.

Different interface circuits have been proposed to harvest energy from EMEH. Full bridge rectifiers (FBR) or voltage multipliers are easy to implement, but their output power is relatively low. They are usually used for the cold-start

* Author to whom any correspondence should be addressed.

process [10]. PWM-based topologies are based on classic PWM converters, such as boost converters [11–13]. They can enhance output power, boost output voltage, and reduce the power dissipation caused by diode voltage drop in the FBR solution. Some designs reuse the EM coil as the inductor [14].

The synchronized switch technique was initially proposed for piezoelectric energy harvesters [15] and later transferred to their EMEH counterparts [5]. The synchronized switch technique can increase the harvested power of piezoelectric devices several times compared with FBRs [16]. Different synchronized switch circuits, such as synchronized electric charge extraction (SECE) [17] and synchronized inversion and charge extraction [18], have been proposed for piezoelectric energy harvesting enhancement. For EMEH, the first synchronized switch circuit is named synchronized magnetic flux extraction (SMFE) [5]. SMFE is designed by taking a reciprocal design of SECE for piezoelectric energy harvesters, i.e. swapping the roles between current and voltage. An improved and self-powered version of SMFE, named synchronous switch energy extraction (SSEE), is proposed in [19]. The measured harvested power of the SSEE circuit is nearly twice the maximum output power of a full-bridge rectifier under the same mechanical excitation. There are also some other self-powered designs of SMFE, including [20] and [21]. The synchronous current inversion (CI) and energy extraction (SCIEE) circuit has been proposed for EMEH [22]. It can harvest more energy than SSEE and PWM-based interface circuits when the quality factor of the energy harvester is relatively high.

In the early PWM-based or synchronized switch interface circuits, external power sources are required to start and power the control circuit [5, 23]. The self-powered and self-start solution of switched-mode interface circuits is crucial for standalone applications.

Some self-powered and self-start solutions have been proposed in recent years. In [20], a self-powered version of SMFE is proposed. The control circuit uses comparators and logic gates. The start-up circuit consists of a half-wave rectifier and a DC–DC regulator IC. The rectified output of the EMEH is fed to an LTC3388, a boost converter IC, to power the control circuit. In [10], a voltage multiplier is employed to cold start the circuit. An additional voltage multiplier is connected to the energy harvester. The output of the voltage multiplier directly powers the control circuit. In [19], the control circuit directly draws power from the load side. The interface circuit in [19] is intrinsically a voltage doubler when all MOSFETs are off. So, the circuit can start without an additional passive rectifier. However, the load must be manually disconnected before cold start-up, or the rectified energy will drain from the load, resulting in a start-up failure.

Existing start-up methods usually utilize passive rectification. For a successful start-up, the passive rectification should be able to output enough power and overcome the leakage current of the control circuit during the start-up process. It should also provide enough power to overcome the surge current at turn-on [24]. Previous papers have reported that the energy output of EMEHs increases drastically after start-up [5, 19]. Therefore, the energy harvesting system has the potential to operate at a lower input voltage, even when the energy output is not enough to power the control circuit before start-up. When a successful cold start-up is somehow achieved, the energy harvesting system will be able to provide sufficient power for the control circuit and operate continuously afterward, thanks to the increased energy output of the EMEH.

In EMEH systems using synchronized switch techniques, existing self-powered solutions are limited to SSEE and SMFE circuits; the SCIEE circuit currently lacks a self-powered and self-start solution. The self-start solutions of existing synchronized switch circuits are based on passive rectification that requires the source's output voltage to be relatively high. This paper proposes a self-start and self-powered method to fill this technical gap. As figure 1 shows, the proposed method introduces an EBR mechanism (EBRM) in the start-up circuit, located between the passive rectification stage and the control circuit. The EBR circuit reduces the leakage of the control circuit before start-up, thereby enhancing the cold-start ability of the system.

2. Operation principle of SCIEE circuit

The operating principle of the SCIEE circuit is briefly presented as an example of a synchronized switch interface circuit and to demonstrate how the proposed self-powered start-up solution can be applied. Figure 2 shows the topology and operation waveform of the SCIEE circuit. L_m is the internal inductance of the EMEH. L_s is a small sensing inductor for current peak sensing. R_s, R_m, and R_h are the ESRs of the corresponding inductors. The quality factor of L_s is set to a large number, so that a zero crossing point (ZCP) of the voltage across the sensing inductor is close to a current peak. The output storage capacitor C_s is much larger than the other capacitors. C_1 and C_2 are for temporary energy transfer. The resonance LC cycle of C_1 and L_m or C_2 and L_m is much smaller than that of the EM source V_{emf}. The source terminals of transistors M_1 and M_2 are connected to ground, allowing the control circuit to drive them directly. More details on the start-up circuit and control circuit are in sections 3 and 4.

In regular operation, transistors M_1 and M_2 are turned on to short-circuit the EMEH. At the negative half-cycle current peak, M_2 switches off for one half of an L_m–C_2 cycle during the CI phase. This instance is also when V_{emf} crosses zero from negative to positive. It forces the current i_m inverses from negative to positive. Then the EMEH is again short-circuited to accumulate more energy inside the EMEH. At zero-crossing instants of V_{emf} from positive to negative, M_1 switches off for approximately one-fourth of an L_m–C_1 cycle during the energy extraction (EE) phase, transferring the energy stored in the EMEH to C_1. The voltage spikes on C_1 and C_2 during the CI and EE phases can power the control circuit. This paper elaborates on the self-powered solution of the SCIEE circuit. Still, the proposed start-up solution also has the potential to be applied to other synchronized switch interface circuits that utilize passive rectification for cold start-up, such as the SSEE circuit [19] or the SMFE circuit [20].

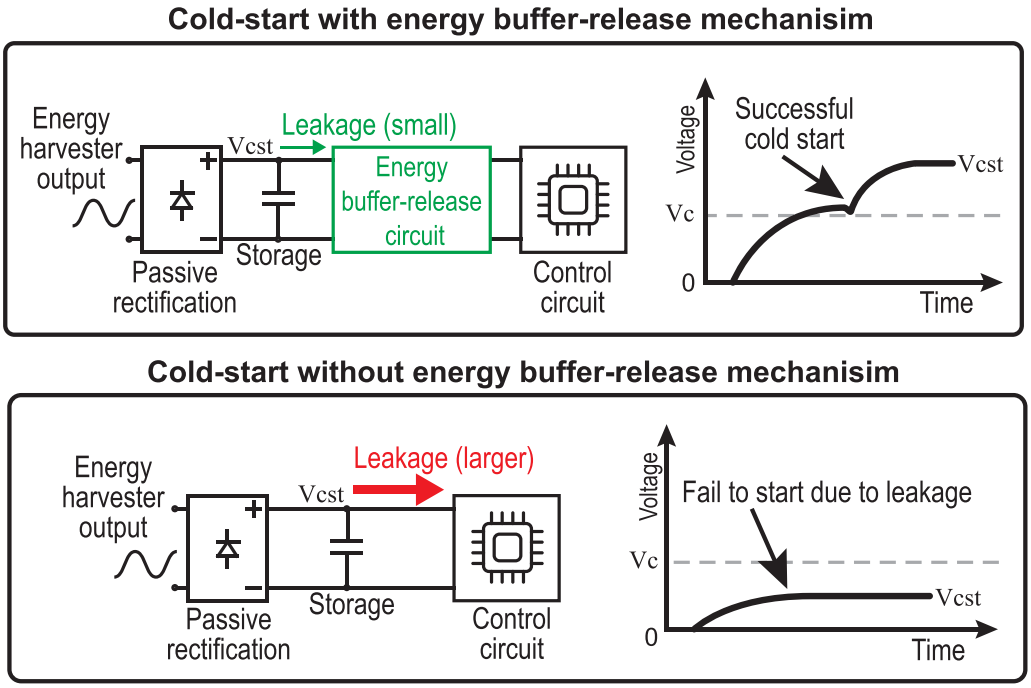

Figure 1. Proposed start-up solution of adding the energy buffer-release (EBR) mechanism in the cold-start process. V_c is the voltage required by the control circuit.

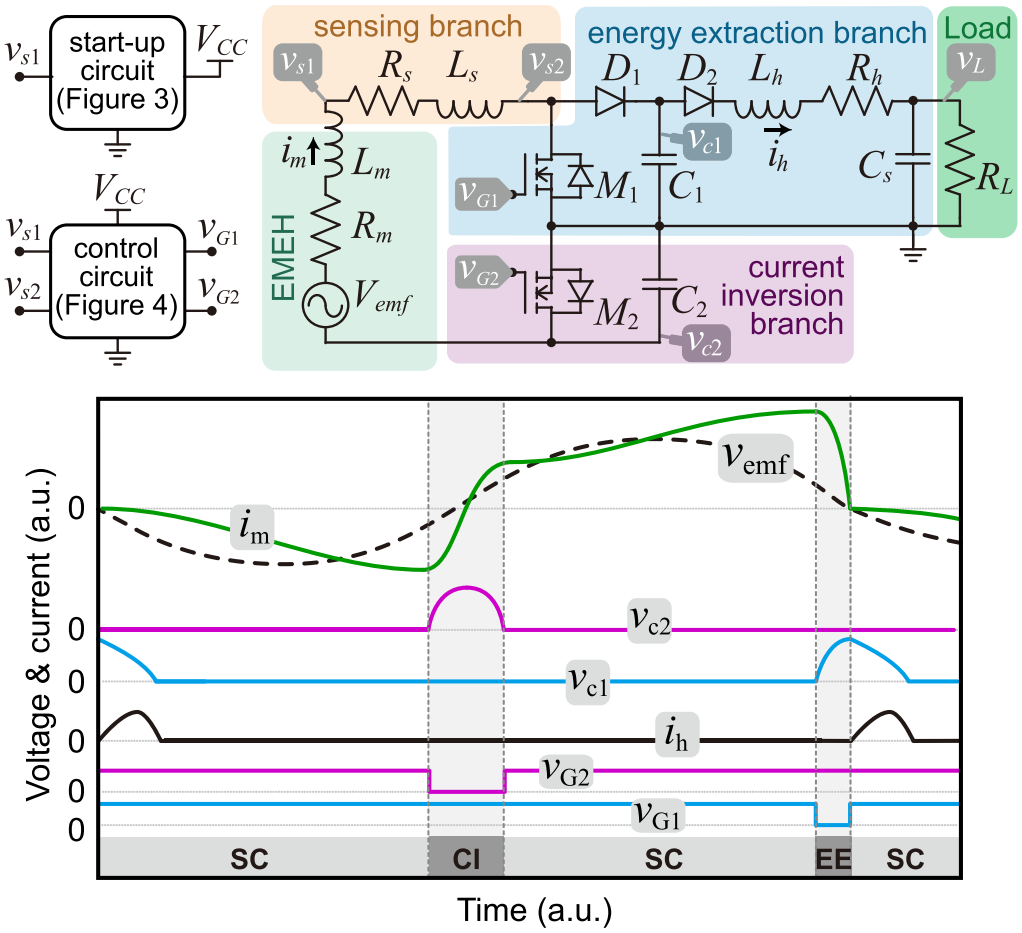

Figure 2. Circuit topology and typical operation waveform of the SCIEE circuit. 'CI' stands for current inversion, 'EE' stands for energy extraction, 'SC' stands for short circuit, and 'a.u.' stands for any unit.

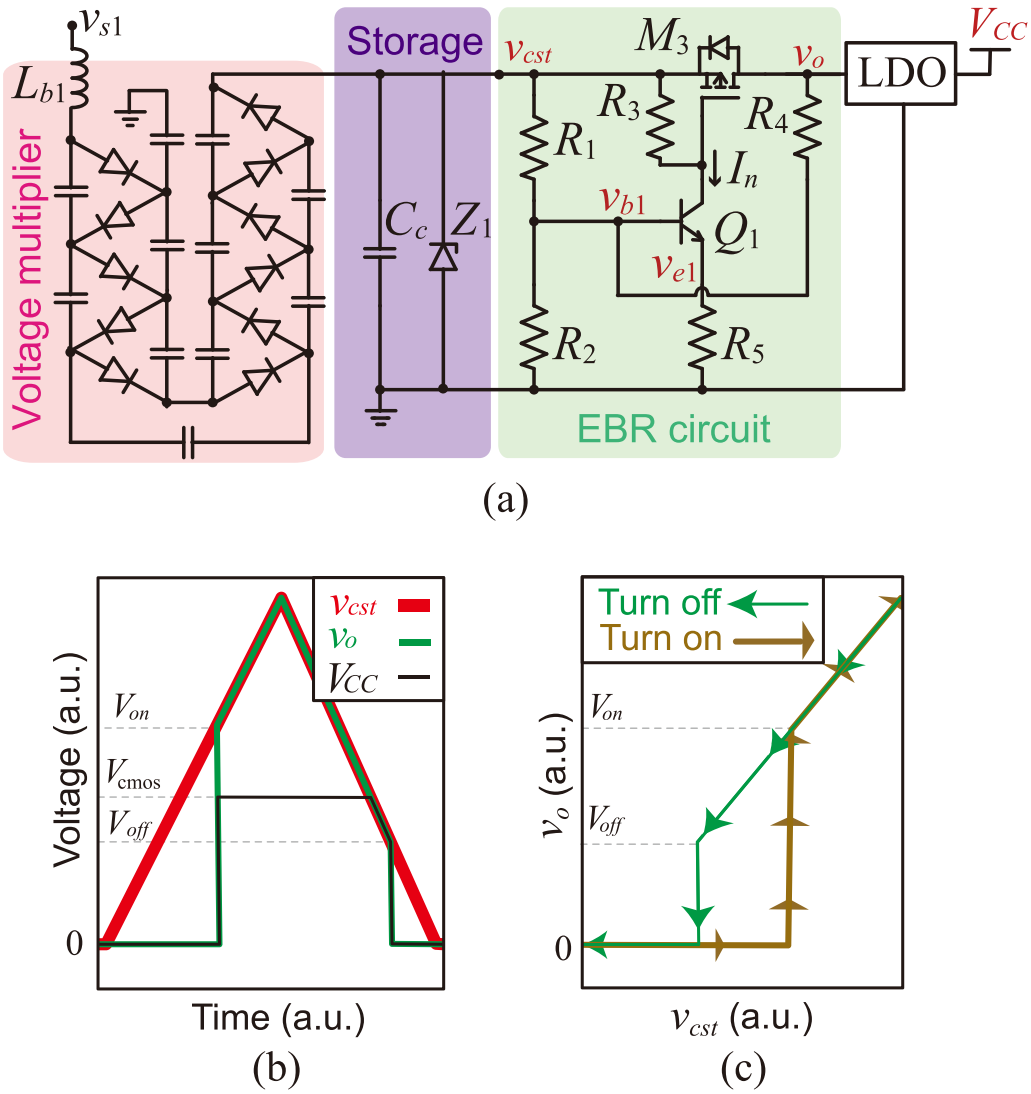

Figure 3. Start-up circuit. (a) Topology. (b) Voltage waveform of the energy buffer-release (EBR) and regulation parts. (c) Voltage hysteresis of the energy buffer-release circuit during the turn-on and turn-off process.

3. Proposed start-up circuit

3.1. Operation principle

As section 2 has discussed, the voltage spikes during the CI and EE phases can power the control circuit. The start-up circuit requires the following features:

- Passively rectify and boost the output voltage during the start-up process.
- Ultra-low power dissipation in the EBR circuit during start-up to operate at low input voltages.
- Capability to withstand high input voltage levels during regular operation.

Considering the above requirements, a start-up circuit is designed based on discrete circuit elements.

Figure 3(a) shows the topology of the proposed start-up circuit. A voltage multiplier boosts the voltage from the v_{s1} node before feeding it to the storage capacitor C_c. The storage capacitor is connected to the EBR circuit. The EBR circuit manages the energy stored in C_c and determines when to activate the rest of the system. This paper uses a six-stage voltage multiplier to achieve a lower start-up voltage. During the cold-start process, C_2 and the body diode of M_1 form a path to charge the voltage multiplier with a pulsed DC voltage from the source. Zener diode Z_1 and inductor L_{b1} are for protection purposes. They can be neglected during start-up because L_{bl}'s impedance is relatively small at the source frequency, and Z_1 is almost an open circuit when the voltage across C_c is below the zener voltage of Z_1.

The output power of the voltage multiplier cannot meet the power requirement of the control circuit when the rest of the system is not operating. So, the EBR circuit buffers the incoming energy in C_c and releases it in a burst to kickstart the system. Figures 3(b) and (c) show the operation waveform and voltage hysteresis of the EBR circuit, respectively. When the input voltage of the EBR circuit, v_{cst}, rises above a predefined

threshold, the switch M_3 turns on, releasing the stored energy to the output. Once activated, the circuit remains on until v_{cst} falls below a lower threshold, at which point it turns off.

The EBRM realized by the proposed circuit is crucial for the self-start-up process. During start-up, C_c is charged through the voltage multiplier, so the voltage across C_c, denoted as v_{cst}, increases. The base-emitter voltage of Q_1 increases with the increasing v_{cst}, so I_n also increases. As more current flows through R_3, the gate-to-source voltage of M3, v_{gs3}, decreases towards a more negative value. When v_{gs3} attains its threshold, M_3 conducts. A small current flows through M_3, and some reaches the base of Q_1 through R_4, causing I_n to increase further. Such a positive feedback loop fully turns on M_3 and Q_1. Then, the energy stored in C_c is released to the input of the low-dropout (LDO) regulator chip. The LDO protects the control circuit from high voltages during regular operation and provides a constant V_{cmos} to start up and power the control circuit. After power is delivered to the control circuit, the system must still be powered for a few source cycles before the main circuit is activated to harvest sufficient power to make ends meet. Therefore, C_c should be sufficiently large to get over this transition. Meanwhile, the voltage hysteresis between the on and off thresholds should ensure sufficient released energy for a successful start-up.

If the kickstart succeeds, the transducer's power will increase drastically. The energy available from the voltage multiplier will allow the control circuit to operate continuously. However, it will also result in a very high v_{cst}. So the zener diode Z_1 and the LDO regulator can protect the control circuit and provide a suitable digital voltage V_{cmos} to the control circuit. L_{b1} can partially block the voltage spikes produced during the CI and EE phases, thereby reducing the energy delivered to the voltage multiplier during regular operation. It helps to reduce the power dissipation on Z_1.

3.2. Theoretical analysis

The turn-on threshold V_{on} is defined as the value of v_{cst} at which v_{gs3} reaches the threshold voltage of M_3. The current I_n at this moment is denoted as $I_{n,cr}$, and the threshold voltage of M_3 is denoted as $V_{th,p}$.

$$I_{n,cr} = |V_{th,p}|/R_3. \tag{1}$$

Since I_n is the collector current of Q_1, the base-emitter voltage difference of Q_1 is given as follows:

$$v_{be1,cr} = v_{b1,cr} - v_{e1,cr} = V_T \ln\left(I_{n,cr}/I_s\right). \tag{2}$$

V_T is the thermal voltage, around 25.9 mV at room temperature. I_s is the constant saturation current of Q_1, which can be extracted from the datasheet or the SPICE simulation models. Given a sufficiently large current gain of Q_1, we have

$$v_{e1,cr} \approx I_{n,cr} R_5. \tag{3}$$

R_1, R_2, R_4, and the input impedance of the LDO form a voltage divider. Since the input impedance of the LDO is much lower than R_4, when M_3 is off, $v_o = 0$. The relationship between V_{on} and $v_{b1,cr}$ can be formulated as follows

$$V_{on} = \frac{R_1 + R_2 \| R_4}{R_2 \| R_4} v_{b1,cr}, \tag{4}$$

where '$\|$' denotes the parallel connecting relation.

Substituting (2)–(3) into (4), the turn-on threshold is formulated as follows

$$V_{on} = \frac{R_1R_2 + R_1R_4 + R_2R_4}{R_2R_4}\left[I_{n,cr}R_5 + V_T \ln\left(\frac{I_{n,cr}}{I_s}\right)\right]. \tag{5}$$

After M_3 conducts, $v_o = v_{cst}$. R_4 is in parallel with R_1. Likewise, the turn-off threshold is as follows:

$$V_{off} = \frac{R_1R_2 + R_1R_4 + R_2R_4}{R_1R_2 + R_2R_4}\left[I_{n,cr}R_5 + V_T \ln\left(\frac{I_{n,cr}}{I_s}\right)\right]. \tag{6}$$

According to (4) and (6), V_{on} is larger than V_{off} given the additional term R_1R_2 in the denominator in (6). One can adjust V_{on} and V_{off} by tuning the resistance of R_1, R_2, and R_4.

3.3. Parameter design process

We should set the turn-on and turn-off thresholds according to the voltage requirement of the control circuit and the capacity of the storage capacitor C_c. The design goal of our setup is to set $V_{on} = 4.8$ V and $V_{off} = 2.4$ V so that the control circuit can be powered around five cycles after start-up when using a 100 μF capacitor. The parameter design process of the EBR circuit is elaborated as an example to demonstrate the parameter design method.

The first step is to determine the transistors to use. We select BSS84PW ($V_{th,p} = -1.5$ V) and MMBT3904 ($I_s = 4.36 \times 10^{-15}$ A) as the transistors since they are low-cost. We start by setting $R_3 = 15\text{M}\Omega$ so that $I_{n,cr} = |V_{th,p}|/R_3$ is around 100 nA. Setting $I_{n,cr}$ small helps to achieve a low quiescent current.

Then, we set R_5 so that v_{b1} is around 0.6 V at a critical point. Solving (2) gives the base-emitter voltage difference of Q1. After solving (2) we have $v_{b1} - v_{e1} = 0.43$ V in this setup. Then, the emitter voltage v_{e1} can be approximated by $v_{e1} = I_{n,cr}R_5$. In this example, we set $R_5 = 1.5\,\text{M}\Omega$ so that solving (2) gives that $v_{b1} = 0.57$ V at critical points. A larger R_5 results in a smaller R_1 and R_4. Resistors larger than 20 MΩ are relatively expensive. R_5 helps to keep the resistor values in a reasonable region.

The next step is to set the current across R_2 to be a few times larger than $I_{n,cr}$, so that the base current of Q1 does not impact the voltage dividing network while keeping the overall quiescent current small. The current across R_2 is given by V_{b1}/R_2. In this case, R_2 is set to 2.4MΩ. After that, R_1 and R_4 can be obtained by substituting values into (5) and (6). The results are $R_1 = R_4 \approx 15\text{M}\Omega$.

4. Switch control circuit

Figure 4 shows the topology of the switch control circuit, and figure 5 shows the operation waveforms of the control circuit. The zero-crossing point of the voltage across L_s, which is

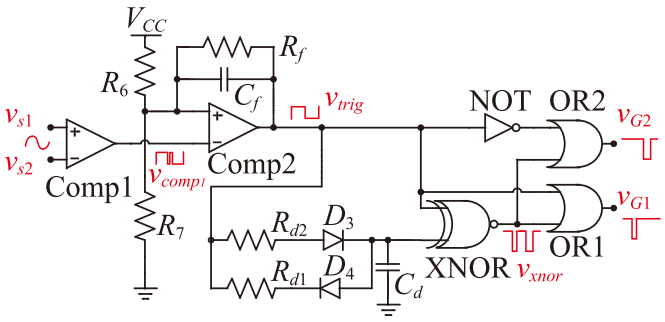

Figure 4. Switch control circuit.

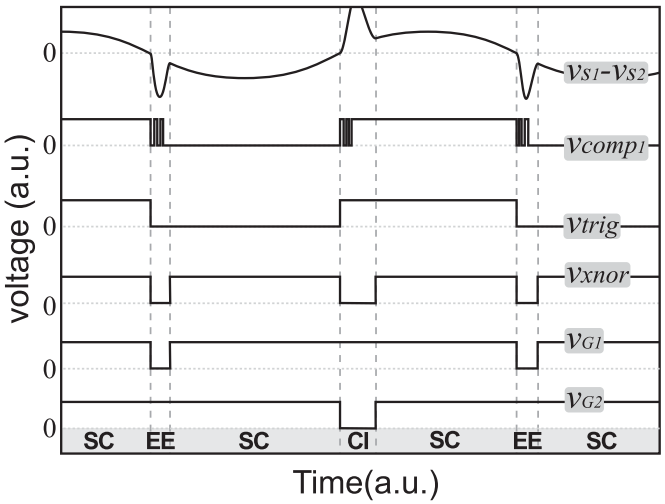

Figure 5. Operation waveforms of the control circuit. CI, EE, and SC correspond to the operational phases in figure 2.

$v_{s1} - v_{s2}$, indicates the peaks and valleys of the current through the sensing inductor [19]. Comparator comp1 detects the zero-crossing points of $v_{s1} - v_{s2}$ and converts them into the rising and falling edges of v_{comp1}. There is some high-frequency noise near the switching points of v_{comp1} because of switching actions and the nature of comparators when operating near the ZCP. Comp2, R_6, R_7, and C_f filter the noise in the output of Comp1 to generate a trigger signal v_{trig}. v_{trig} and a delayed copy of itself are sent to the input of an XNOR gate, to generate short inverted voltage pulses. The output of the XOR gate, v_{xor}, contains the turn-off intervals for both switches. This signal goes through OR gates to generate control signals for M_1 and M_2.

Adjusting R_{d1} and R_{d2} changes the turn-off intervals of gating signal v_{G1} and v_{G2}, respectively. The body diodes of M_2 and M_1 form current paths at the ends of the CI and EE phases. So the turn-off intervals of M_2 and M_1 do not need to be precise. The turn-off interval of M_1 (controlled by v_{G1}) should be longer than the time duration of the EE phase. The voltage drops of diodes D_3 and D_4 have a negligible effect on the delay time. Let the diode voltage drop be V_D. At a rising edge of v_{trig}, D_3 will cause C_d to be charged to $V_{CC} - V_D$ instead of V_{CC}. At a falling edge, C_d will be discharged to V_D instead of 0 V. Because these offsets are symmetric, their effects cancel each other, leaving the delay time essentially unchanged compared to ideal diodes. Therefore, R_{d1} can be determined according to the relation $R_{d1} > \pi\sqrt{(L_m + L_s)C_1}/(1.4C_d)$. Likewise, R_{d2} can be determined according to $R_{d2} > \pi\sqrt{(L_m + L_s)C_2}/(0.7C_d)$.

5. Experiments

5.1. Experiential setup

Printed circuit board assemblies (PCBA) are manufactured to validate the proposed self-start solution. Figure 6 shows the circuit prototype of the start-up circuit. The prototyped start-up circuit powers an SCIEE circuit and its control circuit. Figure 7(a) shows the prototyped system and experimental setup. The EMEH is a rotational one. A brushless DC motor provides mechanical excitation for the EMEH. Figure 7(b) shows the block diagram of the experimental setup. A current probe (CYBERTEK CP8030H) measures the current of the EMEH. The current and voltage waveforms of the system are recorded by an oscilloscope (RIGOL MSO4014). The system's load is different resistors, and the oscilloscope also measures the load voltage V_L. Table 1 lists the components and parameters in the experiment.

5.2. Circuit operation

The first experiment validates the operation of the proposed self-powered solution. The system is not pre-charged, so v_{cst} starts from 0 V at the start of the experiment. The V_{emf} is measured by measuring the open-circuit voltage of the EMEH. Figure 8 shows the measured V_{emf}. V_{emf} is a sinusoidal voltage with an amplitude of 1.85 V and a frequency of 333 Hz. The load R_L is a 325 Ω resistor. Figure 9 shows the voltage and current waveforms in a series of start, shutdown, and restart actions. From the recorded results, the circuit can cold-start as designed. During the cold start-up, the EMEH charges C_c through the voltage multiplier; therefore, v_{cst} slowly rises. During the cold start-up, $V_{CC} = 0$, indicating the EBR circuit keeps the control circuit disconnected in this process. The system self-starts and operates normally when v_{cst} reaches V_{on}. Later, when the EMEH stops, v_{cst} drops below V_{off} shortly after. The EBR circuit shuts down the system. v_{cst} remains at V_{off} until the mechanical input starts again. From the enlarged view on the right of figure 9, the system's operation waveforms agree with the conceptual ones.

To measure the minimum start voltage in this setup, we reduce the rotational speed until the circuit barely manages to cold start. In this experiment, the circuit successfully starts from zero v_{cst} when the EMEH rotates at a lower speed, generating an open-circuit voltage with a 270 Hz frequency and an amplitude of 1.35 V. Figure 10 shows the cold start process under these conditions. In figures 9 and 10, v_{cst} is recorded through a 10:1 resistor dividing network with a total resistance of 100 MΩ to reduce the leakage current of the voltage probe, so 1 V on the oscilloscope corresponds to 10 V of the actual value.

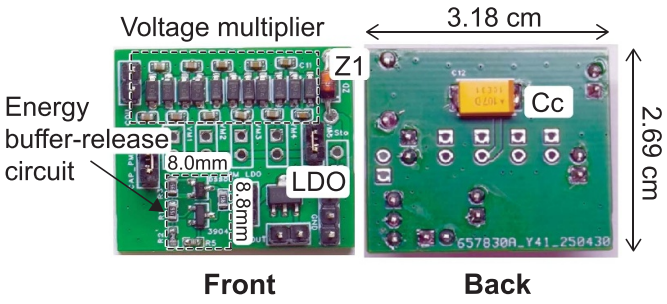

Figure 6. Prototyped start-up circuit.

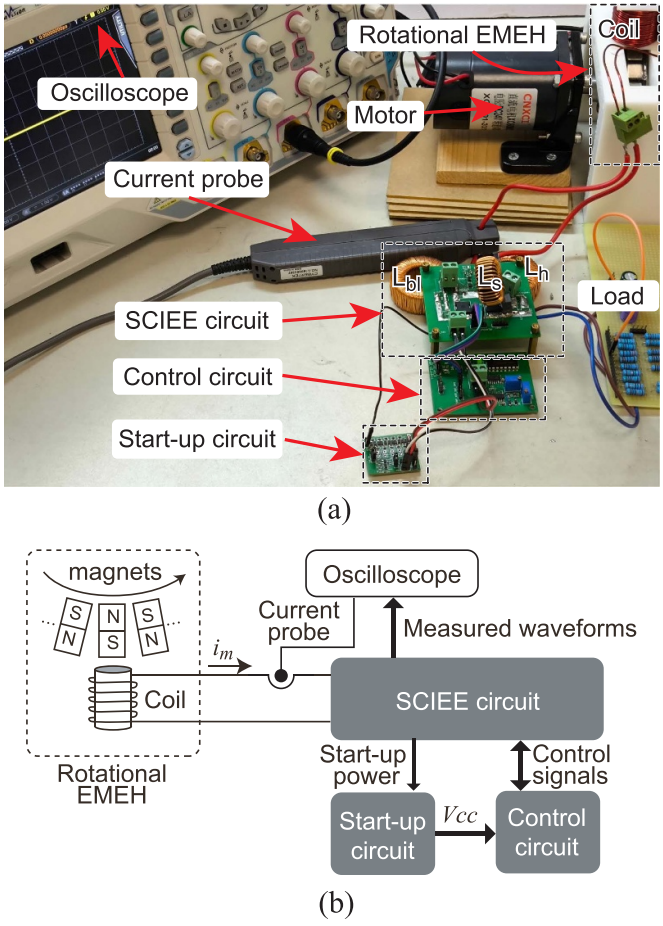

Figure 7. Experimental setup. (a) Overview of test setup. (b) Block diagram.

5.3. Evaluation of the proposed EBR circuit

The second experiment evaluates the proposed EBR circuit. In this experiment, the EBR circuit is isolated from the system. A 20 kΩ resistor is connected between v_o and ground as the load. A triangular wave is fed to v_{cst} to observe the behavior of the EBR part. v_o is measured under different R_1 and R_4. We extract the turn-on and turn-off voltage thresholds from the recorded v_o waveform. Figure 11 shows one of the recorded waveforms when $R_1 = R_4 = 15$ MΩ. The transient response of the EBR circuit agrees with the theoretical prediction.

The measured turn-on and turn-off thresholds of the EBR circuit are compared to theoretically calculated and simulated values. The simulated voltage thresholds are obtained from SPICE simulation results. Figure 12(a) shows the results under different R_1. Figure 12(b) shows the results under different R_4. The theory, simulation, and experiment show good agreement.

We measure the input leakage current of the proposed energy buffer–release circuit before turn-on to evaluate its dissipation during start-up. The leakage current is measured using the Keysight CX3322A device current analyzer. With $R_1 = R_4 = 15\,\text{M}\Omega$ and an input voltage of 2.4 V, the leakage current of the proposed energy buffer–release circuit is 0.14 μA. Under identical conditions, the control circuit draws around 64.4 μA. These results confirm that the energy buffer–release circuit exhibits significantly lower input leakage before start-up, thereby enhancing the cold-start ability, as illustrated in figure 1.

Using the same measurement setup, we also measured the input leakage current of LTC3108 and LTC3588 at 2.4 V. The LTC3108 and LTC3588 integrate rectification, cold-start, energy management, and voltage regulation, making them commonly used in energy harvesting applications [25–27].

Table 1. Components and parameters in the experiment.

Component	Value / Type
L_m	1.2 mH (ESR $R_m = 0.27\ \Omega$)
L_h,L_{bl}	15 mH (ESR $R_h = 2.4\ \Omega$)
L_s	0.2 mH (ESR $R_s = 38$ mΩ)
C_1, C_2, C_c, C_s	2 μF, 2 μF, 100 μF, 700 μF
R_1, R_2, R_3, R_4, R_5	15 MΩ, 2.4 MΩ, 15 MΩ, 15 MΩ, 1.5 MΩ
C_d, R_{d1}, R_{d2}	1 nF, 150 kΩ, 300 kΩ
R_6, R_7, R_f, C_f	120 kΩ, 120 kΩ, 10 MΩ, 20 nF
Diodes D_1, D_2	1N4004
Voltage multiplier diodes	MBR0530
Voltage multiplier capacitors	2.2 μF
Comparators	LMC7211BIM5
LDO	HT7544
OR, XNOR, NOT gates	CD4071, CD4077, CD4049
Zener diode Z_1	1N4745A
Q_1,M_3	MMBT3904, BSS84
M_1, M_2	IPT015N10N5

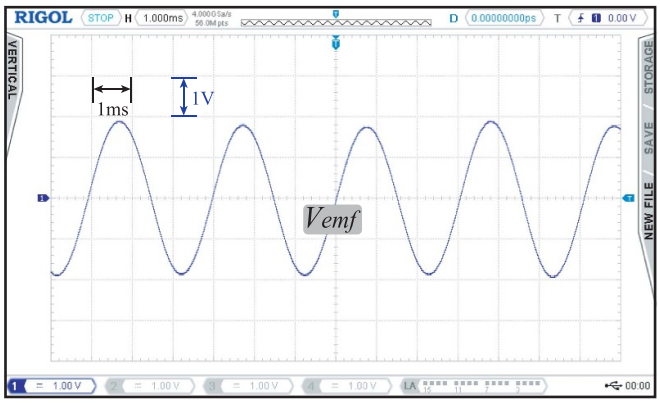

Figure 8. Measured open-circuit voltage of the EMEH in the experiment.

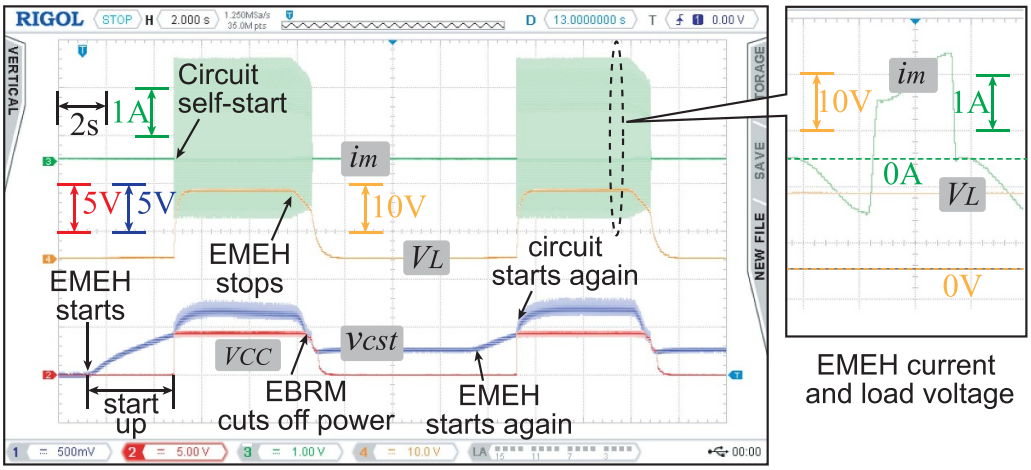

Figure 9. Voltage and current waveform in the experiment during cold start and stop transients. V_{L}, i_{m}, V_{cst} and V_{CC} corresponds to figure 2.

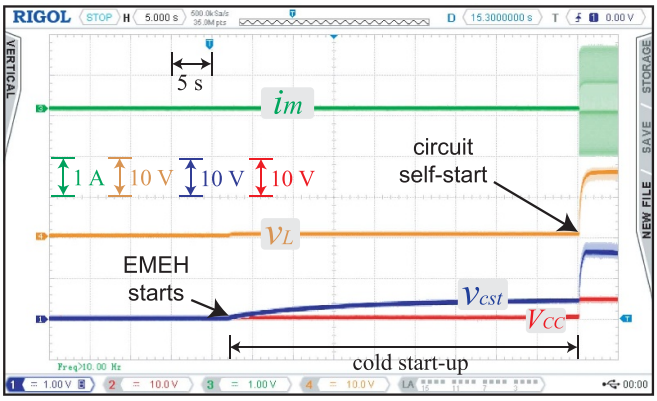

Figure 10. The recorded voltage and current waveform in the cold start process at 1.35 V input.

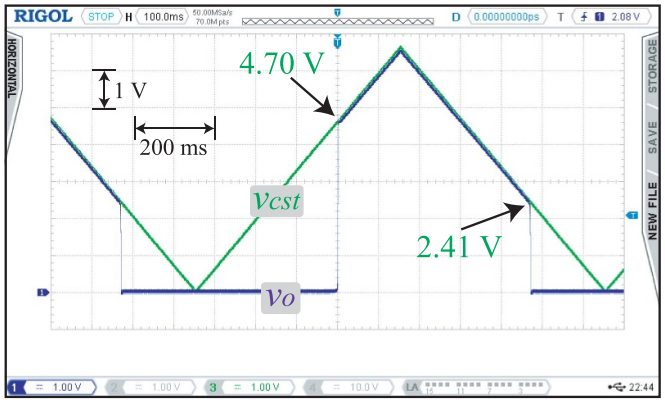

Figure 11. Measured voltage transients of the energy buffer-release circuit. $R_1 = R_4 = 15\ \mathrm{M\Omega}$.

Since the proposed energy buffer–release circuit is designed for cold-start and energy management, we compare the cold-start and energy management performance of the proposed energy buffer–release circuit with those of the two ICs' corresponding features. The LTC3108 begins to operate at 2.5 V, so we measure the input leakage at 2.4 V input to evaluate the cold-start capability. The leakage measured at V_{AUX} pin of LTC3108 is 6.6 μA, and the leakage measured at V_{IN} pin of LTC3588 is 0.48 μA. Table 2 shows a summary of the comparison results.

The LTC3108's energy management strategy involves charging an auxiliary capacitor (C_{aux}) at its V_{AUX} pin and then discharging it into the load once the voltage across C_{aux} exceeds 2.5 V. The activation of the discharge path increases the input current to a level comparable to the load current. If the load current demand exceeds the input current, the voltage cannot continue to rise, preventing a successful start-up. As a result, the LTC3108 cannot release energy in a burst for kickstarting. Therefore, the LTC3108 is typically used only with ultra-low-power loads. The proposed circuit maintains low leakage and supports energy buffering to higher voltage levels before release, enabling reliable cold-start under less favorable load conditions.

The LTC3588 supports energy buffer–release behavior via its built-in under-voltage lockout (UVLO) feature. However, the available turn-on thresholds are fixed at either 4.05 V or 5.05 V. The voltage hysteresis is fixed at three levels, ranging from 1.03 V to 1.38 V. The LTC3588 adjusts the turn-on and turn-off thresholds based on the programmed output voltage, so these thresholds are not independently adjustable. On the other hand, the proposed EBR circuit offers a broader and adjustable hysteresis window. The turn-on and turn-off thresholds can be set by selecting resistors. So, a smaller buffer capacitor C_{c} can achieve the same energy release for kickstarting. Regarding start-up capability, the proposed circuit demonstrates a lower input leakage of 0.14 μA compared to the LTC3588's 0.48 μA.

Compared to the fully integrated LTC3108 and LTC3588, the proposed energy buffer–release circuit achieves lower quiescent leakage and more adjustable turn-on and turn-off thresholds. The design is more cost-effective, even when considering the additional costs of rectification and voltage-regulation circuitry. Its configurable threshold levels and minimal overhead make it a flexible and cost-effective solution for implementing cold-start and energy management functions in energy harvesting systems.

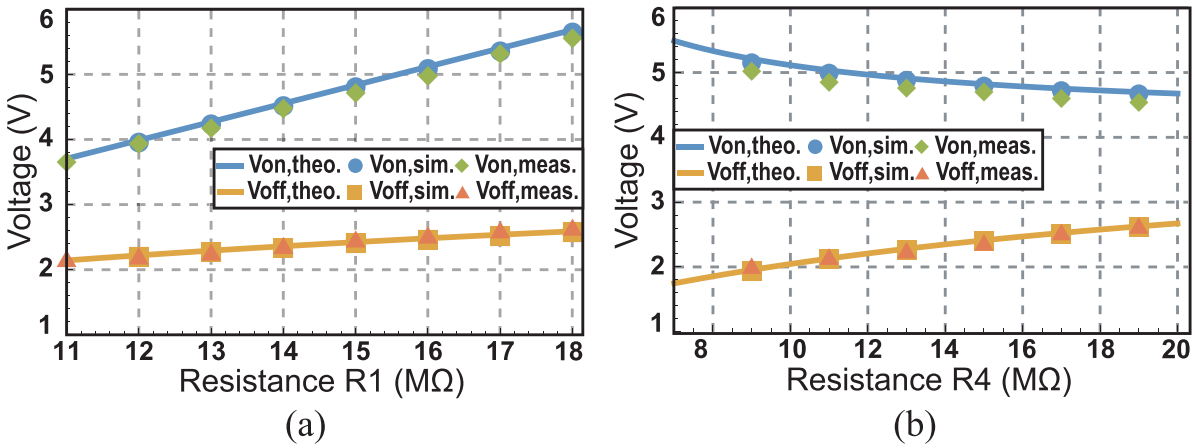

Figure 12. Theoretical, simulated, and measured voltage thresholds of the energy buffer-release circuit. (a) Results under different R_1 when $R_4 = 15$ MΩ. (b) Results under different R_4 when $R_1 = 15$ MΩ.

Table 2. Comparison between proposed energy buffer-release circuit and commercial ICs commonly used for energy harvesting.

Design	Buffer-release capability	Leakage current (μA)	Turn-on threshold	Voltage hysteresis	Max input voltage (V)	Relative cost
LTC-3108	—	6.6	Fixed	—	6	High
LTC-3588	Yes	0.48	Fixed[a]	Fixed[a]	18	High
Proposed	Yes	0.14	Adjustable	Adjustable	20	Low

[a] User-selectable between two or three values. Turn-on threshold can be 4.05 or 5.05 V, and voltage hysteresis can be 1.03, 1.17, or 1.38 V.

5.4. Energy harvesting performance

The third experiment compares the energy harvesting performance with and without this self-start and self-powered solution. The amplitude and frequency of V_{emf} in this experiment are also 1.85 V and 333 Hz, the same as the first experiment. We measure the output power by measuring the output voltage at different resistive loads. Another measurement is performed after removing the start-up circuit and using an external power supply (GW Instek GPD-3303D) to power the control circuit. We also recorded the output power of an externally powered SSEE circuit [19] fabricated with the same circuit components for comparison. The three measurements are under the same mechanical excitation. Figure 13 shows the harvested power in the three cases. The self-start and self-powered scheme utilizes a small portion of the harvested energy to realize the self-start-up and control. This portion is relatively small. The SCIEE circuit implemented with the proposed self-power solution can still harvest more energy than the SSEE circuit, even when the SSEE circuit is externally powered.

We calculate the total power dissipation of the start-up and control circuit by evaluating the difference in output power between the self-powered and externally powered cases. The total power dissipation of the auxiliary circuits is 29.6 mW at low output voltage and 59.3 mW at high output voltage, respectively. The power consumption increases with output voltage because, at higher output voltage, the peak value of v_{c1} also increases [22]. Therefore, more power is delivered to C_c, causing Z_1 to dissipate more power and limit the increase in v_{cst}, thereby protecting the control circuit from overvoltage.

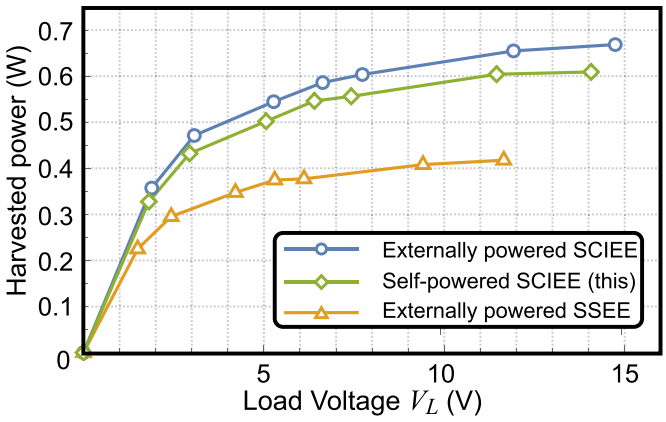

Figure 13. Measured output power. Circles are the output of the externally powered SCIEE circuit. Diamonds are the output of the SCIEE circuit, self-powered by the proposed solution. Triangles are the output of an externally powered SSEE circuit for comparison.

In the externally powered case, the measured power consumption of the control circuit is around five mW. So the start-up circuit dissipates 24.6–54.3 mW, depending on the load voltage. We use SPICE simulation to estimate the power consumption of different parts in the start-up and control circuits. Table 3 shows the breakdown of the power consumption of the start-up and control circuits obtained from the simulation. The LDO and Z_1 consume most power. The EBR circuit consumes only around 46 μW. The simulation result is close to the experimental one.

Table 3. Estimated power consumptions of the start-up and control circuits.

Component	Power (mW)[a]
Energy buffer-release part	46.4×10^{-3}
Voltage multiplier	8.03
Zener diode D1	21.95
LDO	12.92
Control	04.98
L_{bl}	4.15
Total	52.07

[a] Simulation condition: source amplitude is 1.85 V @ 333 Hz; load voltage is 14 V.

Table 4. Comparison of interface circuits for EMEH enhancement and their cold-start solutions.

Circuits	Cold-start architecture	Minimum start voltage	Battery-free	Self-powered	Self start-up
Boost [23]	Battery	—	—	Yes	—
SMFE [20]	Rectification and LTC3388	3.5	Yes	Yes	Yes
SSEE [19]	Rectification	2.5	Yes	Yes	—
SMFE+SECE [21]	—	2.96[a]	Yes	Yes	Yes
This	Rectification with EBRM	1.35	Yes	Yes	Yes

[a] A higher voltage amplitude is required for proper energy output.

Table 4 compares the proposed system with some relevant designs for EMEH. The interface circuit in [23] uses an auxiliary battery to realize self-sustaining operation. It can start at any transducer voltage, but the battery needs to be precharged. The circuit in [20] rectifies the transducer voltage using a half-wave rectifier and utilizes the LTC3388 to boost the rectified voltage. The interface circuit proposed in [19] does not require any additional start-up circuit; however, the load must be manually disconnected before the start-up process. The hybrid circuit in [21] uses an inductor with a relatively high inductance to generate the control signals. It does not need external circuits for control or start-up. But it requires a higher transducer voltage to operate.

6. Conclusion

Kinetic energy harvesting using EMEHs offers a promising approach to realize self-powered IoT systems in sensing and monitoring scenarios. Interface circuits play a key role in such self-powered systems. Prior studies have shown that the synchronized switch technique considerably improves the output power. Self-power and self-start functionality are essential for the standalone applications of such synchronized switch interface circuits.

This paper proposes a self-start and self-powered solution. It can start and power a SCIEE circuit to enhance the output power of EMEHs. The self-start circuit requires neither precharged batteries to run nor a manual load connection after the energy is ready, and it helps the circuit to cold-start at a lower input voltage.

The start-up circuit employs an EBRM with a circuit consisting of two off-the-shelf transistors and several resistors. The EBR circuit demonstrates ultra-low power consumption. The EBRM helps the system to cold-start at low-voltage input conditions when passive rectification alone can not power the control circuit. Experiments demonstrate that the theoretical values of the EBR circuit and experimental results align well. The input leakage current of the EBR circuit, measured at 2.4 V, is 0.14 μA. The leakage current is lower than that of the control circuit, as well as commercial ICs LTC3108 and LTC3588 under the same operating conditions.

Experimental results have validated the operation of the proposed self-start solution. The circuit can self-start at a relatively small input voltage amplitude of 1.35 V. It achieves the lowest start-up voltage among existing self-powered battery-free synchronized switch interface circuits for EM transducers. The proposed system can harvest more energy in experiments than an externally powered SSEE interface circuit. When the load voltage is 14 V, the EBR circuit dissipates 46 μW. The power consumption of the cold start circuit and control circuit accounts for 8.8% of the harvested power.

Overall, the proposed self-powered solution realizes self-contained operation of an SCIEE energy harvesting circuit. The start-up solution enhances the system's start-up ability at low input voltage levels. Furthermore, the proposed method of adding the EBRM also provides new insights when designing the cold-start functionality of interface circuits for EMEHs.

Data availability statement

The data cannot be made publicly available upon publication because no suitable repository exists for hosting data in this field of study. The data that support the findings of this study are available upon reasonable request from the authors.

Conflict of interest

The authors declare no conflict of interest.

Acknowledgments

This research is supported by the National Natural Science Foundation of China (No. 62271319).

ORCID iDs

Jiacong Qiu 0009-0007-4774-7872
Junrui Liang 0000-0003-2685-5587

References

[1] Nabavi S F 2018 Anooshiravan Farshidianfar and Aref Afsharfard. Novel piezoelectric-based ocean wave energy harvesting from offshore buoys *Appl. Ocean Res.* **76** 174–83
[2] Fu H, Mei X, Yurchenko D, Zhou S, Theodossiades S, Nakano K and Yeatman E M 2021 Rotational energy harvesting for self-powered sensing *Joule* **5** 1074–118
[3] Ali A, Shaukat H, Bibi S, Altabey W A, Noori M and Kouritem S A 2023 Recent progress in energy harvesting systems for wearable technology *Energy Strategy Rev.* **49** 101124
[4] Beeby S P, Torah R N, Tudor M J, Glynne-Jones P, O'Donnell T, Saha C R and Roy S 2007 A micro electromagnetic generator for vibration energy harvesting *J. Micromech. Microeng.* **17** 1257
[5] Arroyo E and Badel A 2011 Electromagnetic vibration energy harvesting device optimization by synchronous energy extraction *Sens. Actuators A* **171** 266–73
[6] Lombardi G, Lallart M, Kiziroglou M and Yeatman E M 2020 A piezoelectric self-powered active interface for AC/DC power conversion improvement of electromagnetic energy harvesting *Smart Mater. Struct.* **29** 117002
[7] Zhang H, Zhou S, Xu H and Zhou S 2023 A high-performance rotational electromagnetic energy harvester based on magnetic plucking: design, simulation and experiment *Mech. Syst. Signal Process.* **204** 110778
[8] Wang T, Lv H and Wang X 2024 Development of an electromagnetic energy harvester for ultra-low frequency pitch vibration of unmanned marine devices *Appl. Energy* **353** 122072
[9] Cao H, Kong L, Tang M, Zhang Z, Wu X, Lu L and Li D 2023 An electromagnetic energy harvester for applications in a high-speed rail pavement system *Int. J. Mech. Sci.* **243** 108018
[10] Dinulovic D, Shousha M, Al-Batol M, Zafar T, Bickel J, Ngo H-D and Haug M 2021 Dual-rotor electromagnetic-based energy harvesting system for smart home applications *IEEE Trans. Magn.* **57** 1–5
[11] Wang L, Wang H, Fu M, Xie Z and Liang J 2022 Three-port power electronic interface with decoupled voltage regulation and MPPT in electromagnetic energy harvesting systems *IEEE Trans. Ind. Appl.* **58** 2144–54
[12] Shousha M, Dinulovic D, Haug M, Petrovic T and Mahgoub A 2020 A power management system for electromagnetic energy harvesters in battery/batteryless applications *IEEE J. Emerg. Sel. Top. Power Electron.* **8** 3644–57
[13] Dayal R, Dwari S and Parsa L 2011 Design and implementation of a direct AC-DC boost converter for low-voltage energy harvesting *IEEE Trans. Ind. Electron.* **58** 2387–96
[14] Chen J, Peng H, Feng Z and Kang Y 2021 A GaN BCM AC–DC Converter for Sub-1 V electromagnetic energy harvesting with enhanced output power *IEEE Trans. Power Electron.* **36** 9285–99
[15] Guyomar D, Badel A, Lefeuvre E and Richard C 2005 Toward energy harvesting using active materials and conversion improvement by nonlinear processing *IEEE Trans. Ultrason. Ferroelectr. Freq. Control* **52** 584–95
[16] Brenes A, Morel A, Juillard J, Lefeuvre E and Badel A 2020 Maximum power point of piezoelectric energy harvesters: a review of optimality condition for electrical tuning *Smart Mater. Struct.* **29** 033001
[17] Lefeuvre E, Badel A, Richard C and Guyomar D 2005 Piezoelectric energy harvesting device optimization by synchronous charge extraction *J. Intell. Mater. Syst. Struct.* **16** 865–76
[18] Lallart M, Wu W-J, Hsieh Y and Yan L 2017 Synchronous inversion and charge extraction (sice): a hybrid switching interface for efficient vibrational energy harvesting *Smart Mater. Struct.* **26** 115012
[19] Xie Z, Teng Li, Wang H, Liu Y, Fu M and Liang J 2023 A self-powered synchronous switch energy extraction circuit for electromagnetic energy harvesting enhancement *IEEE Trans. Power Electron.* **38** 9972–82
[20] Jia S, Zeng C, Shi G, Hong C, Han J and Xia Y 2023 A self-powered synchronous magnetic flux extraction interface for electromagnetic energy harvesting *Microelectron. J.* **140** 105943
[21] Jia S, Zeng C, Shi G, Xu J, Li Y, Xia H and Xia Y 2023 A self-powered interface circuit for simultaneous piezoelectric and electromagnetic energy extraction *IEEE Trans. Power Electron.* **38** 10640–50
[22] Qiu J, Wang H, Liu Y, Fu M and Liang J 2024 A synchronous current inversion and energy extraction circuit for electromagnetic energy harvesting enhancement *IEEE Trans. Circuits Sys. I* **71** 5471–81
[23] Dayal R, Dwari S and Parsa L 2011 A new design for vibration-based electromagnetic energy harvesting systems using coil inductance of microgenerator *IEEE Trans. Ind. Appl.* **47** 820–30
[24] Stark B H, Szarka G D and Rooke E D 2011 Start-up circuit with low minimum operating power for microwatt energy harvesters *IET Circuits Devices Syst.* **5** 267–74
[25] Guo S, Gao S, Jin L, Du X, Yin Z, Wu Q and Li Z 2021 Mechanism, theory and application research of a rotating electromagnetic energy harvester suitable for multi-directional excitation *J. Phys. D: Appl. Phys.* **55** 085503
[26] Orfei F, Mezzetti C B and Cottone F 2016 Vibrations powered lora sensor: an electromechanical energy harvester working on a real bridge *2016 IEEE SENSORS* pp 1–3
[27] Hamid R and Yuce M R 2017 A wearable energy harvester unit using piezoelectric–electromagnetic hybrid technique *Sens. Actuators A* **257** 198–207